

Explaining the Evolution of Ion Velocity Distributions at a low activity Comet

A. Moeslinger^{1,2}, H. Gunell², H. Nilsson^{1,2}, S. Fatemi², and G. Stenberg
Wieser^{1,2}

¹Swedish Institute of Space Physics, 981 28 Kiruna, Sweden

²Department of Physics, Umeå University, 901 87 Umeå, Sweden

Key Points:

- Hybrid simulations with the Amitis code for a low activity comet show the formation of a half-open induced magnetosphere.
- The velocity distributions of solar wind protons form partial rings in the simulation as previously reported by observations.
- Backtracing the cometary ions in the tail shows that the shape of their velocity distributions is driven by electric field structures.

Corresponding author: A. Moeslinger, anja.moeslinger@irf.se

Abstract

At a low activity comet the plasma is distributed in an asymmetric way. The hybrid simulation code Amitis is used to look at the spatial evolution of ion velocity distribution functions (VDFs), from the upstream solar wind to within the comet magnetosphere where the solar wind is heavily mass-loaded by the cometary plasma. We find that the spatial structures of the ions and fields form a highly asymmetric, half-open induced magnetosphere. The VDFs of solar wind and cometary ions vary drastically for different locations in the comet magnetosphere. The shape of the VDFs differ for different species. The solar wind protons show high anisotropies that occasionally resemble partial rings, in particular at small cometocentric distances. A second, decoupled, proton population is also found. Solar wind alpha particles show similar anisotropies, although less pronounced and at different spatial scales. The VDFs of cometary ions are mostly determined by the structure of the electric field. We perform supplementary dynamic particle backtracing to understand the flow patterns of solar wind ions that lead to these anisotropic distributions. This tracing is needed to understand the origin of cometary ions in a given part of the comet magnetosphere. The particle tracing also aids in interpreting observed VDFs and relating them to spatial features in the electric and magnetic fields of the comet environment.

1 Introduction

Comets are known to be one of the most diverse objects in our solar system when it comes to the spatial scales of their magnetospheres (Edberg et al., 2024). This is due to the variability in their outgassing rate, which is a measure of their activity and describes the rate at which the ices near the surface of the comet nucleus sublimate. Because of the small size of comet nuclei, these particles are not gravitationally bound and escape into space. Comet outgassing rates depend on various parameters. To an extent it is an intrinsic quantity individual to each comet since it depends on the nucleus size, surface structure, and nucleus composition. However, it also depends on the heliocentric distance of the comet: comets at their perihelion have outgassing rates that are orders of magnitude higher than when they are several AU away from the sun. The neutral gas profile of a comet is frequently modelled based on the assumption of spherically symmetric outgassing where it follows a $1/r^2$ profile (r : cometocentric distance) (Haser, 1957). This neutral gas gets ionised by photoionisation, charge exchange, and electron-impact-ionisation, and creates newborn cometary ions (e.g. Galand et al., 2016). For the solar wind, this cloud of cold ions presents an obstacle: the solar wind gets mass-loaded (Biermann et al., 1967). The result of this plasma interaction between the solar wind and the cometary ions depends on the solar wind parameters as well as the altitude profile of newborn cometary ions. At very low comet activity the solar wind only gets lightly deflected (Broiles et al., 2015; Behar et al., 2016). At intermediate to high activity the comet magnetosphere may contain several plasma boundaries (Mandt et al., 2016), including a solar wind ion cavity (Behar et al., 2017; Nilsson et al., 2017) and a bow shock (Neubauer et al., 1986). The comet studied in most detail so far has been comet 67P/Churyumov-Gerasimenko (Taylor et al., 2017), visited by the Rosetta spacecraft (Glassmeier et al., 2007). A review of the observations of the comet plasma environment is found in Goetz et al. (2022).

For intermediate activity at comet 67P the first stage of a bow shock was observed (Gunell et al., 2018) and a magnetosheath formed (Williamson et al., 2022). Regions of heated solar wind were observed sporadically during low-to-intermediate activity (Goetz et al., 2021). The most detailed study so far of the observed velocity distribution functions (VDFs) at a low-to-intermediate activity comet for a period with very broad solar wind proton energy spectra revealed that the protons formed partial ring structures in velocity space (Moeslinger, Stenberg Wieser, et al., 2023). The ions making up such

a partial ring come from many different directions. In an environment small compared to an ion gyroradius these ions may have passed through very different regions of the comet - solar wind interaction region. Until the Comet Interceptor mission (Jones et al., 2024) delivers the first multi-point measurements of a comet, we have no observations that simultaneously cover different parts of the comet plasma environment. To fully understand how such ion velocity distribution functions form and how we can interpret them, we need to turn to models.

Numerical models of space plasmas can be split into 3 categories: magnetohydrodynamic (MHD) models, hybrid models, and fully kinetic particle-in-cell (PIC) models. Their applicability depends on the spatial scales of the physical processes one is interested in. MHD models are especially suited for studying large-scale objects where both ions and electrons can be considered fully magnetised. Typical subjects of MHD models are plasma interactions between the solar wind and planets with strong intrinsic magnetic fields, like at Earth and Jupiter. High-activity comets, such as comet 1P/Halley at perihelion, can also be modelled using MHD models. Fully kinetic PIC models are found on the other end of the scale, where even kinetic effects of electrons play an important role in the physics of the system. However, the computational effort limits the use case to modelling of small-scale objects, for examples comets with very low activity, and small moons (e. g., Phobos). Hybrid models, like the one used in this paper, are able to fill the gap in between by modelling the kinetic effects of ions. They are typically used to model solar wind - plasma interactions at objects like low-to-intermediate activity comets (Gunell et al., 2024), Mars (Wang et al., 2023), as well as the Earth’s Moon (Holmström et al., 2012).

By studying the velocity distribution functions (VDFs) of the plasma species, both in observations and using models, we are able to see the transfer of energy from particles to fields and vice versa. Anisotropic VDFs can be the source of various plasma waves and an indicator for various plasma processes. Examples include pick-up ion distributions (Coates et al., 1989) and ion conics resulting from ion heating and the mirror force (André & Yau, 1997). Kinetic effects are relevant for many processes in space plasmas, in particular at small scales and at boundaries. At a low-outgassing comet, like comet 67P, the environment is continuously changing. The typical scales are smaller than the ion gyroradius, making the environment dominated by kinetic effects. Analysing the VDFs is necessary to understand the physical processes, both in observations as well as models.

2 Methods

2.1 Hybrid Model Simulations

The core of this study is a hybrid simulation of the comet magnetosphere using Amittis (Fatemi et al., 2017). Amittis is a GPU-based three-dimensional simulation code for space plasmas. The model is well-established and has been applied to various bodies. The results have been verified with spacecraft observations at comet 67P (Gunell et al., 2024), Mars (Wang et al., 2023), Ganymede (Fatemi et al., 2022), and Mercury (Aizawa et al., 2021). It uses the hybrid particle-in-cell (PIC) approximation: ions are modelled as (macro-)particles, while the electrons are modelled as massless fluid. The electron fluid acts as a charge neutralising background. By treating the ions as particles there is no restriction regarding their distribution in phase space. The electromagnetic fields \mathbf{E} and \mathbf{B} are computed using the generalised Ohm’s law (Equation 1) and Faraday’s law (Equation 2). The current density \mathbf{J} is approximated by Ampere’s law neglecting the displacement current from $\frac{\partial \mathbf{E}}{\partial t}$ (see Equation 3).

$$\mathbf{E} = -\frac{\mathbf{J}_I \times \mathbf{B}}{\rho_I} + \frac{\nabla \times \mathbf{B}}{\mu_0} \times \frac{\mathbf{B}}{\rho_I} - \frac{\nabla p_e}{\rho_I} + \frac{\eta}{\mu_0} \nabla \times \mathbf{B} \quad (1)$$

$$\frac{\partial \mathbf{B}}{\partial t} = -\nabla \times \mathbf{E} \quad (2)$$

$$\mathbf{J} = \frac{\nabla \times \mathbf{B}}{\mu_0} \quad (3)$$

113 with $p_e \propto n_i^\gamma$, $\gamma = 5/3$. A more detailed description of the hybrid model equations
114 can be found in Fatemi et al. (2017) and Ledvina et al. (2008).

115 Table 1 gives an overview of the various simulation parameters. The simulation re-
116 sults are stored on a three-dimensional cartesian grid with a spatial resolution of 25 km.
117 Each grid point has a cell of dimensions $(25 \text{ km})^3$ associated with it. The entire simu-
118 lation space has a size of $7000 \text{ km} \times 12\,000 \text{ km} \times 16\,000 \text{ km}$ ($x \times y \times z$). In the model ref-
119 erence frame the comet is fixed at $(0, 0, 0)$. The x-axis points towards the sun, and the
120 upstream solar wind magnetic field is oriented along $+y$, that is, $\mathbf{B} \perp \mathbf{v}_{\text{SW}}$, with a strength
121 of 3 nT. The time resolution of the simulation is 0.5 ms. We include three different ion
122 species in the simulation: solar wind protons (H^+), solar wind alpha particles (He^{2+}),
123 and a cometary ion species with mass 18 amu (H_2O^+). Ions are implemented as so-called
124 macro particles, where one such macro particle represents a fixed number of “real” ions
125 of a certain species. Solar wind ions are injected with a drifting Maxwell-Boltzmann dis-
126 tribution at the upstream boundary, the parameters for both SW species are given in
127 Table 1. The initialised cometary ions are based on a spherically symmetric neutral pro-
128 file that decreases with radial distance r from the comet (Haser, 1957). Photoionisation
129 is the only considered generation mechanism, and the local ion production rate $P(r)$ de-
130 pends on the comet outgassing rate Q and the photoionisation rate $\nu^{h\nu, \text{ioni}}$:

$$P(r) = \frac{Q\nu^{h\nu, \text{ioni}}}{4\pi u_r r^2} \quad (4)$$

131 with $Q\nu^{h\nu, \text{ioni}} = 1.08 \times 10^{20} \text{ s}^{-2}$ and the neutral expansion rate $u_r = 700 \text{ m s}^{-1}$. In-
132 creasing the number of particles improves the numerical stability and the statistical prop-
133 erties of the simulation. As a tradeoff, the computational workload also increases.

Table 1. Simulation parameters

	SW H^+	SW He^{2+}	cometary ions (H_2O^+)
Macro particle weight	1.3×10^{18}	1×10^{17}	1×10^{18}
Upstream speed	430 km/s	430 km/s	-
Upstream density	1 cm^{-3}	0.05 cm^{-3}	-
Upstream temperature (in K)	$61.1 \times 10^3 \text{ K}$	$214 \times 10^3 \text{ K}$	-
Upstream temperature (in eV)	5.3 eV	9.2 eV	-

134 2.2 Velocity Distribution Functions

135 The velocity distributions (VDFs) are calculated from the macro particles. Since
136 there is only a small number of particles per cell, the VDFs are integrated in space and
137 time to achieve better statistical properties. Each VDF is calculated for a box of size $(100 \text{ km})^3$
138 and therefore contains 64 simulation cells. It is desirable not to count the same macro
139 particle many times in the same place to ensure that the particles are mostly uncorrel-
140 ated. For our conditions we can meet this requirement by sampling only every 200th
141 time step. We integrate for a total of 30k simulation time steps (15 s), which results in
142 a total of 151 individual samples. We note that very slow particles may still be counted
143 multiple times. The macro particles are binned in 3D velocity space. This result is nor-
144 malised by macro particle weight (w ; different for each species), number of time steps
145 (N_{ts}), box volume (ΔV), and velocity bin volume (ΔV_v):

$$f(\mathbf{x}, \mathbf{v}) = \frac{N_{\text{MP}}(\mathbf{x}, \mathbf{v}) w}{\Delta V \Delta V_v N_{ts}} \quad (5)$$

146 $N_{\text{MP}}(\mathbf{x}, \mathbf{v})$ is the number of macro particles in the phase space volume $\Delta V \Delta V_v$ at (\mathbf{x}, \mathbf{v}) .
 147 The velocity bin width Δv is identical for all three axes, $\Delta v^3 = \Delta V_v$. It is adjusted for
 148 each species based on particle statistics and can be seen in Figure 3. Finally, the result
 149 is integrated along the v_y axis, which gives the presented 2D histograms.

150 2.3 Particle Tracing

151 The code for the particle tracing (Moeslinger & Gunell, 2024) is an adapted ver-
 152 sion of the particle tracing code used in Gunell et al. (2015). It uses the electric and mag-
 153 netic fields from the hybrid simulations to advance the particle positions and velocities
 154 for each timestep. The grid size and cell resolution is identical to the Amitis grid. The
 155 electric field is corrected by the resistive term to obtain the field \mathbf{E}_P that is applied to
 156 the particle motion: $\mathbf{E}_P = \mathbf{E} - \eta \mathbf{J}$. Since the plasma environment around the comet
 157 is highly dynamic, we extended the code to support particle tracing in time-variable fields.

158 The initial particles for the tracing are directly sampled from the macro particles
 159 in the Amitis simulation at a specific time step (here: 300k). After initialising the fields
 160 for the tracing from this time step, they are dynamically updated after each timestep
 161 (10ms) as the simulation progresses. The different ion species are simulated separately.
 162 The integration scheme for the particle motion (Boris (1970), see also for example Ledvina
 163 et al. (2008)) is symmetric in time, which makes it possible to not only forward- but also
 164 backtrace particles, depending on the sign of the tracing time step. In this paper we only
 165 used the backtracing capabilities.

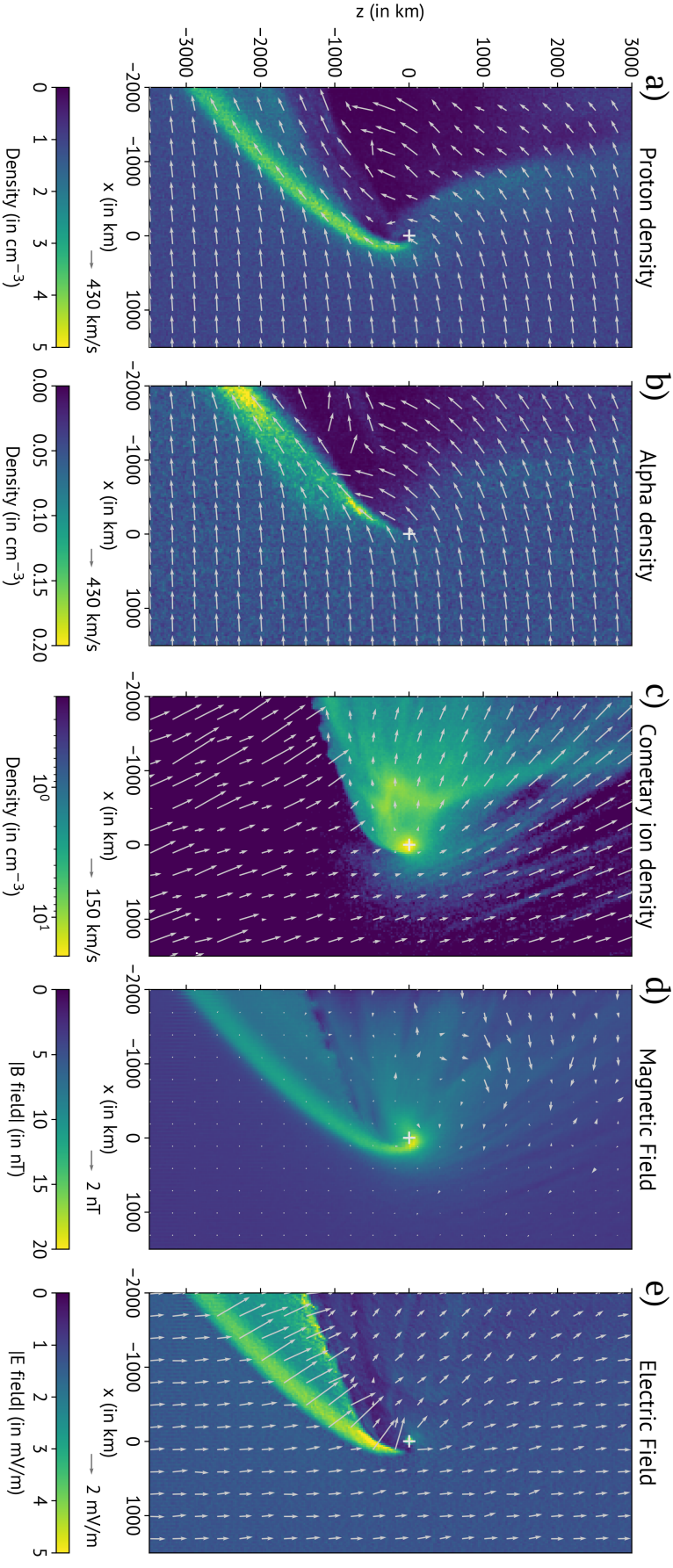
166 3 Results

167 In this section we give an overview of the simulation results of both the hybrid model
 168 and the particle tracing. Both models are fully three-dimensional (see Section 2), and
 169 all results are presented in the model reference frame. We will focus on the $x-z$ plane,
 170 perpendicular to the upstream magnetic field. The upstream convective electric field in
 171 this reference frame is along $+z$, and the $z = 0$ -plane divides the space into a $+E$ ($z >$
 172 0) and a $-E$ ($z < 0$) hemisphere. In all figures we show the slice located at $y = 0$, but
 173 additional figures for $y \neq 0$ and different projections can be found in the supporting
 174 information S1 (for the spatial structures) and S2 (for the VDFs).

175 3.1 Overview of the comet magnetosphere

176 Figure 1 presents an overview of the comet environment as simulated by Amitis.
 177 Panels a - c show the density and projected velocity (that is, v_x, v_z) of the three ion species
 178 included in the simulation (a: Protons, b: Alpha particles, and c: Cometary ions), while
 179 panels d and e show the magnetic and electric fields, respectively. All panels show the
 180 slice at $y = 0$ (y_0). The y_0 -slice is calculated as an average of the two grid layers cen-
 181 tred at ± 12.5 km. The plasma environment behaves symmetrically around y_0 . This sym-
 182 metry improves the statistical qualities of the shown data without compromising the spa-
 183 tial resolution. At the right edge of each panel (towards $+x$) the plasma approaches its
 184 undisturbed upstream state. The results show a highly asymmetric plasma structure with
 185 respect to the upstream electric field. The solar wind ions are deflected towards $-z$, while
 186 the cometary ions are accelerated towards $+z/-x$. The magnetic field piles up in front
 187 of the comet.

188 The mean velocities of both solar wind species are almost completely anti-sunward
 189 in the upstream region, with only a slight deflection (Figure 1a and b). At $x = 1000$ km, $z =$
 190 0 the deflection is 9.8° for the protons and 6.4° for the alpha particles. Following the flow



191 of the protons (Figure 1a) downstream in the $-E$ hemisphere we note that they are in-
 192 creasingly deflected until they reach a plasma boundary where the density is increased
 193 above a factor of 4 with respect to the upstream value. Similar structures have been seen
 194 in other simulations, see for example Gunell et al. (2018) and Koenders et al. (2016, Sim-
 195 ulation F), although both simulations model comet 67P at higher activity closer to the
 196 Sun. The mean velocity is along the plasma boundary structure, and no significant de-
 197 celeration is seen. Far behind the main density enhancement region the protons are de-
 198 pleted. This transition is sharp close to the nucleus and becomes more gradual further
 199 downstream. At $x = -1500$ km the density remains elevated by a factor of 3. The nose
 200 of the plasma boundary appears at $x = 200$ km, $z = -250$ km. In the $+E$ hemisphere
 201 the deflection of protons is stronger than in the $-E$ hemisphere, and there is a decel-
 202 eration of the protons. A transient plasma boundary with a slight density enhancement
 203 ($\approx 1.2 - 1.5$ times the upstream value) can be seen (e. g. $x = -700$ km, $z = 500$ km).
 204 While the plasma boundary in the $-E$ hemisphere remains stationary, the one in the
 205 $+E$ hemisphere slightly varies in position and intensity over time. At the boundary the
 206 protons get deflected towards $\pm y$ (out of the plane shown), and the density drops close
 207 to 0. The remaining ions in the downstream region have a mean velocity close to or above
 208 the upstream solar wind velocity.

209 The overall plasma structure of alpha particles (Figure 1b) is similar to that of the
 210 protons. Due to the lower number of particles per cell in the simulation compared to the
 211 protons the results appear more noisy; this is purely a statistical / numerical effect. In
 212 the $-E$ hemisphere the alpha particles are deflected and form a plasma boundary with
 213 density enhancements by a factor of 2.5–4 with respect to the upstream values. The
 214 peaks in the density enhancement around $x = -300$ km and $x = -1800$ km are sta-
 215 tionary features. The location of the plasma boundary is shifted in the $-x$ direction by
 216 a few hundred kilometres with respect to the proton density enhancement. The width
 217 is broader than the proton boundary. Downstream of the density enhancement the al-
 218 pha densities are depleted almost instantly. Comparing the deflection of protons and al-
 219 pha particles in the $+E$ hemisphere we find that the alpha particles are less strongly de-
 220 flected, which is in agreement with in-situ observations close to the nucleus (Behar et
 221 al., 2017). There is no significant deceleration of alphas when moving downstream, and
 222 no clear plasma boundary is formed. The depletion due to deflection out of the y_0 -plane
 223 is more gradual.

224 The plasma structure of the cometary ions (Figure 1c) is dominated by the imposed
 225 newborn ion profile and the electric field structures (shown in Figure 1e). The highest
 226 densities occur at the nucleus. In the $+E$ hemisphere the ions are accelerated towards
 227 $+z$ along the electric field. At larger distances from the comet the anti-sunward veloc-
 228 ity component increases due to a change of the electric field direction and the progress-
 229 ing gyration. Upstream of the nucleus, at $z \approx 0$, the ion density decreases with increas-
 230 ing radial distance from the nucleus, and the ion speed increases. Downstream of the nu-
 231 cleus there is a large region where the density only varies between $3-10 \text{ cm}^{-3}$. The ve-
 232 locities are mostly anti-sunward, and the speeds increase with radial distance as well.
 233 The spatial boundary of this region at smaller z coincides with the upper boundary of
 234 the electric field enhancement (cf. Figure 1e). At even smaller z values the cometary ion
 235 density becomes very small, and the ions behave like pick-up ions in the solar wind elec-
 236 tric field. The mean velocities depend on the exact gyration phase of the sampled par-
 237 ticles. At $x \geq 0, z > 1000$ km wave-like structures appear in the cometary ion den-
 238 sity.

239 Panel d (Figure 1) shows the magnetic field. In the $-E$ hemisphere the increase
 240 in magnetic field strength is mostly in the y -direction and the solar wind ion flow is along
 241 the magnetic field enhancement structure. The magnetic field increases up to 15 nT at
 242 the nose of the pile-up structure and stays at about 12 nT further away from the nucleus.
 243 The pile-up structure coincides with the density enhancement seen in the protons (Fig-

244 ure 1a). The maximum magnetic field strength is 20 nT within 125 km from the nucleus,
 245 on the $+x/+z$ side of the comet. A close-up of this region is also shown in Figure 2.
 246 Downstream of the nucleus the magnetic field strength drops to about 8 nT within 300 km
 247 of the nucleus, and remains relatively constant further tailwards. In the entire $-E$ hemi-
 248 sphere the B_x and B_z components of the magnetic field are negligible. This is not true
 249 for the $+E$ hemisphere: wave-like structures appear (similar to Koenders et al., 2016)
 250 and B_x and B_z become non-zero. The magnetic field is still enhanced with respect to
 251 the upstream value, and varies between 5 and 10 nT. The vortices occurring in the mag-
 252 netic field (see e. g. at $x = -1800$ km, $z = -1200$ km) are likely numerical artefacts
 253 due to the low number of macro particles in this region. The “ripples” parallel to the
 254 simulation boundary at $x = -2000$ km are also simulation artefacts. Due to the low
 255 amplitude and spatial extent neither are expected to affect the described features in the
 256 plasma. They are outside any areas covered in the subsequent analysis.

257 The electric field (panel e) is mostly dominated by the convective electric field and
 258 is also highly asymmetric. In the $-E$ hemisphere it is enhanced due to the pile-up of the
 259 magnetic field. The direction remains perpendicular to the flow direction of the solar wind
 260 ions. The maximum electric field strength is above 5 mV/m and is found close to the nu-
 261 cleus (at $x = 0, z = -400$ km). This is a factor of 4 larger than the upstream value of
 262 1.3 mV/m. Further away from the nucleus the electric field is still enhanced to 4 mV/m.
 263 We define two E -field boundaries for reference in this paragraph: the lower boundary
 264 marks the transition between the almost undisturbed upstream solar wind electric field
 265 and the initial E -field enhancement. The upper boundary is towards $+z$ from the lower
 266 boundary where the electric field strength drops to values around or below the upstream
 267 value. The upper boundary of the enhancement region (at -1200 km $\leq z \leq -800$ km)
 268 coincides with the drop in the density of cometary ions. In the local proton reference frame
 269 the electric field at this boundary is pointing in the opposite direction. Its magnitude
 270 is about 1 mV/m, with a width of 100 km across the boundary (results obtained via Lorentz
 271 transformation using the local proton velocity and magnetic field; data not shown). A
 272 few hundred kilometres above this boundary, the electric field strength drops to values
 273 below the upstream electric field. In the $+E$ hemisphere the electric field is rotated up
 274 to 45° around $-y$ at $x < 0$ due to the deflection of SW ions and the flow of cometary
 275 ions. There is no enhancement of the electric field strength in this area. Close to the nu-
 276 cleus (< 50 km from the centre) there is an ambipolar electric field. Directly upstream
 277 of the nucleus there is a small region that is shielded from the SW electric field. The elec-
 278 tric field strength in this shielded region drops to about 0.2 mV/m.

279 3.2 Velocity Distribution Functions

280 For evaluating the velocity distribution functions (VDFs) we identified different re-
 281 gions of the magnetosphere. Figure 2 shows a close-up of the magnetic field where the
 282 different regions can be seen. Within each region the VDFs continuously evolve. The pre-
 283 sented VDFs should thus be seen as a typical example for the region and will not be iden-
 284 tical away from the sampling location. All sampling locations for each species are labelled
 285 and indicated with boxes in Figure 2.

286 Proton VDFs are calculated at six different locations, P1-P6. In the $+E$ hemisphere
 287 P1 samples the downstream ($x < 0$) region while P2 samples the upstream ($x > 0$)
 288 region. P3 is located in the area of maximum magnetic field pile-up close to the nucleus.
 289 This region can also be compared to observational results. In the $-E$ hemisphere one
 290 sampling point is located in the region downstream of the magnetic pile-up boundary
 291 (P4). P5 is upstream of the nose of the proton density enhancement, while P6 samples
 292 the region right at the proton density enhancement. The VDFs of the alpha particles
 293 are obtained in the downstream region (A1) and the alpha density enhancement (A2).
 294 A2 is slightly offset towards $-x$ compared to P6 due to the shift in spatial structures be-
 295 tween the protons and alpha particles. A3 is in the same area as P3, for comparison with

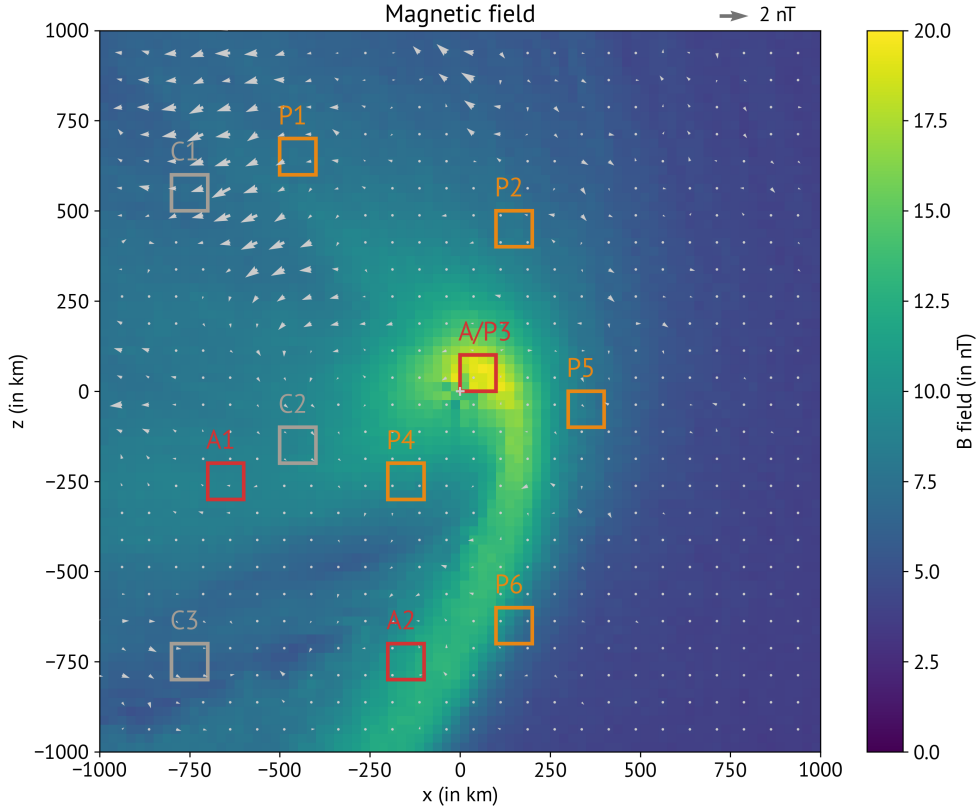


Figure 2. Close-up of the magnetic field at timestep 300k (background, same quantities as Figure 1, panel d). The boxes show the sampling locations of the VDFs for the different species; P: protons (orange), A: alpha particles (red), C: cometary ions (grey). Each box has a side length of 100 km and is centred around $y = 0$.

296 observations. The alpha particle VDFs in the remaining $+E$ hemisphere are almost Maxwellian,
 297 therefore no additional results are shown. Cometary ion VDFs are only analysed in the
 298 downstream region at three different locations. The samples are taken at sufficient dis-
 299 tance from the nucleus so that the observed cometary ion velocity distributions had time
 300 to evolve. A continuous sampling of VDFs from $x \in [-800 \text{ km}, 800 \text{ km}]$ and $z \in [-800 \text{ km}, 800 \text{ km}]$
 301 for $y = 0 \text{ km}$, $y = -300 \text{ km}$, and $y = -600 \text{ km}$ for all three species can be found in
 302 the supporting information S2. This include the upstream region of only slightly deflected,
 303 Maxwellian-shaped solar wind.

304 Figure 3 shows the calculated VDFs for the highlighted sampling locations. The
 305 box labels and box centre locations are given at the top of each VDF. The lowest value
 306 on the colour bar represents the occurrence of exactly one macro particle in the calcula-
 307 tion of the VDF. It can help to get a statistical estimate of the likelihood of occurrence,
 308 i. e., bins with such low values are not statistically significant. However, those with a VDF
 309 one-two orders of magnitude higher are.

310 In panel P1 (top left) two distinct proton populations can be identified. The main
 311 population (that with highest phase space density) is highly deflected compared to the
 312 upstream SW. Its shape is slightly anisotropic compared to a perfect Maxwellian distri-
 313 bution. The second population has a much lower phase space density and an anti-sunward
 314 velocity of about $v_x \approx 550 \text{ km/s}$. The main population at P2 is less deflected, and the

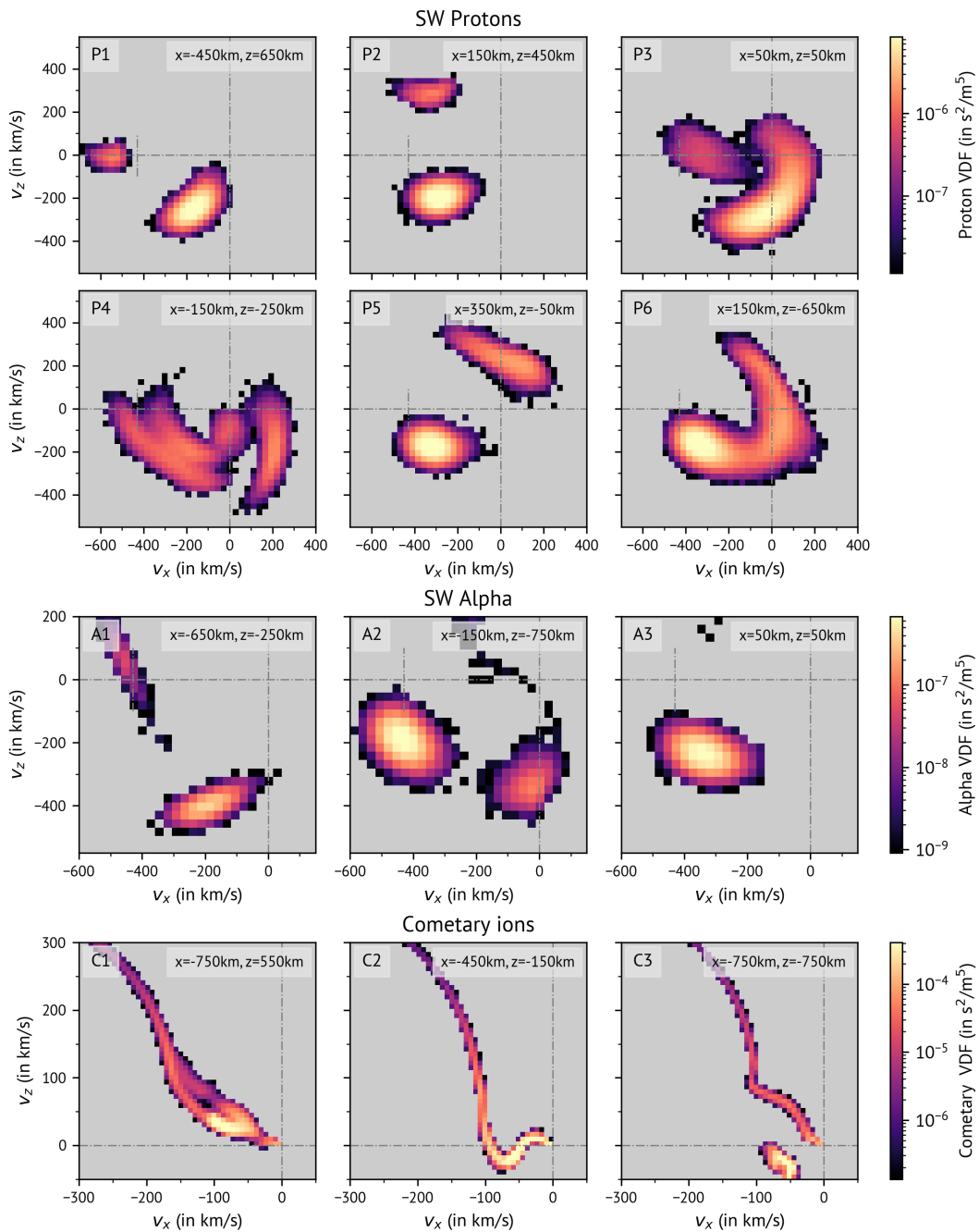


Figure 3. Velocity distribution functions (VDFs) for the locations shown in Figure 2. The box labels and centre box locations can be found at the top of each VDF. The VDFs are integrated over the y -axis and averaged over the entire box. The dash-dotted lines indicate the velocities $v_x = 0$, $v_z = 0$, and $v_x = 430$ km/s (upstream solar wind speed; short vertical line, solar wind species only). For more information see text.

315 secondary population has a slightly higher phase space density and a significant flow component in the z -direction. Close to the nucleus (P3) the main population forms a partial ring. The deflection from the upstream SW direction ranges from 45° to up to above 270° , although the phase space density decreases for very high deflection angles. A sec-

316
317
318

319 onary population moving roughly in the anti-sunward direction is also observed. The
 320 velocity spread of the secondary population here is quite large, and its speed is typically
 321 below the upstream solar wind speed. Upstream the nose of the proton density enhance-
 322 ment (P5) the main population is a slightly deflected Maxwellian distribution with a mean
 323 velocity slightly lower than the upstream SW velocity. The secondary population has
 324 a much broader velocity distribution and the mean velocity is directed in the opposite
 325 direction. At sampling location P6 (right at the proton plasma boundary) the distribu-
 326 tion is similar to P5. However, the secondary population is much broader, and the two
 327 populations begin to merge. The VDF calculated at P4, downstream of the boundary,
 328 shows four distinct populations. All four populations have much lower phase space den-
 329 sities than any of the main populations observed in the other sampling locations.

330 There are two alpha particle populations in the region downstream of the alpha den-
 331 sity enhancement (Panel A1, third row of Figure 3). Their VDFs have a non-Maxwellian
 332 shape. The phase space density of both populations is much lower than the upstream
 333 SW alpha particle density (compare to Panel A3). At the alpha particle density enhance-
 334 ment A2 a slightly deflected main population is seen. Its mean speed of 442.7 km/s ex-
 335 ceeds the upstream SW speed. The secondary population is deflected by 90°, which is
 336 less than the protons in the comparable VDF (P6). Both populations still have a roughly
 337 Maxwellian shape. There is a 3rd population at positive v_z , but due to low counts we
 338 do not expect it to be a permanent feature of the VDF in this region. Sampling the VDF
 339 close to the nucleus (A3) we only observe one population. It is deflected by about 30°
 340 and slightly anisotropic.

341 The bottom row of Figure 3 shows the VDFs of the cometary ions. A radially ex-
 342 panding population is only observed within 100 km of the nucleus (data not shown). All
 343 three sampled VDFs (C1 - C3) have a high-velocity component that appears circular.
 344 It starts at $v_x = -180$ km/s, $v_z = 100$ km/s for C1, at $v_x = -100$ km/s, $v_z = 0$ for C2,
 345 and at $v_x = -120$ km/s, $v_z = 80$ km/s for C3. For velocities below these values, the
 346 VDFs are intricately shaped but different for all three cases. None of them resembles a
 347 Maxwellian distribution. Only at C3 we see two distinct low-velocity populations: one
 348 connected to the higher velocity part with positive v_z , and another one with higher in-
 349 tensity and less velocity spread at negative v_z . At C1 and C2 the different parts of the
 350 VDF are all connected. Whether these VDFs are comprised of different overlapping pop-
 351 ulations cannot be said from this plot.

352 **3.3 Particle Tracing**

353 We selected some of the VDFs presented in the previous section for the particle back-
 354 tracing: P1, P3, P5, A2, and all cometary VDFs (C1, C2, C3). The main goal is to iden-
 355 tify differences in the ion flow patterns for the different parts of the VDF. From the dif-
 356 ferent individual trajectories we assess what regions in the magnetosphere they pass through.
 357 With the solar wind particles one main point is to identify the upstream regions where
 358 the particles originated. This also gives the associated upstream VDF of these particles,
 359 which is a subset of the Maxwellian-shaped VDF of the upstream solar wind. For the
 360 cometary ions it helps to understand where the particles that make up different parts
 361 of the VDF were born.

362 **3.3.1 Solar Wind Ions**

363 Tracing results for both solar wind species are presented in the same format for all
 364 chosen sampling locations (Figures 4 to 7). Panel a shows a density map of the trajec-
 365 tories of all ions back-traced from the sampling location (see boxes defined in Figure 2).
 366 The ions are sampled at a single Amitis time step (at $t = 300$ k). The density is summed
 367 over the entire y -axis. Upstream at $x = 4000$ km the velocities of the ions are measured
 368 at different z locations by cubic probes. The probes are separated by 250 km along the

369 z axis and their locations are indicated by the black boxes. The probes are labelled in
 370 descending order, i. e., the top probe is probe 1. Panel b shows the VDFs for all probe
 371 locations. It should be noted that the measured ions in each probe only show what part
 372 of the upstream SW population can reach the tracing origin. The complete distribution
 373 at this point is a 3D Maxwellian, as defined in the simulation parameters for the hybrid
 374 model. Since the relation of the tracing and probe densities to typical physical quanti-
 375 ties are rather unimportant, they are not normalised and presented only in arbitrary units.
 376 Panel c shows the trajectories of several individual particles. The line colours refer to
 377 the different observed velocities at the starting position. The initial velocity for each par-
 378 ticle is seen in panel d, on top of the time-averaged VDF at this observation point (same
 379 as shown in Figure 3).

380 Figure 4 shows the back-tracing results of observation point P3 (protons; close to
 381 the nucleus). The major part of all particles enters the observation region after a deflec-
 382 tion of about 90° from the upstream solar wind flow and only passes through the $+E$
 383 hemisphere. A smaller portion shows more evolved flow patterns and is observed after
 384 completing a full gyration loop (see panels a and c). All traced particles originate within
 385 1500 km along the z -axis at the probe location. The majority of the particles are back-
 386 traced to within 1000 km and are observed in Probes 4 and 5. The VDFs of the individ-
 387 ual probes (Panel b) are similar for all probes: they have a spread of about 100 km/s along
 388 v_z , centred at $v_z = 0$. The spread in the v_x direction is only about 50 km/s for an in-
 389 dividual probe. Its mean ranges from $v_x \approx -490$ km/s at probe 2 to $v_x \approx -360$ km/s
 390 at probe 7. Probes 4 and 5 have mean v_x velocities at about the SW speed. Exceptions
 391 from this elongated main cluster occur at higher v_x . For the main population there is
 392 a correlation between observed velocity and upstream origin along z (panels c and d).
 393 Particles with lower energy and higher deflection originate from larger z compared to
 394 their higher energetic, less deflected counterparts. The gyration pattern of the particles
 395 belonging to the secondary population is especially clear in panel c (blue trajectories,
 396 for initial velocities see panel d). They are reflected right at the nose of the proton den-
 397 sity enhancement region. The upstream origin of these particles is the same as the peak
 398 of the main population.

399 Figure 5 shows the back-tracing results of observation point P1 (protons; down-
 400 stream in the $+E$ hemisphere). Two distinct flow patterns are seen. The upstream ori-
 401 gin of the main population at the probe location is within about 1500 km along the z -
 402 axis, with the major part originating within 500 km (see panels a and c). The correla-
 403 tion between observed velocity (energy) and reconstructed origin along z is similar to
 404 what is seen at P3 (Figure 4). All particles of this population are at an initial stage of
 405 gyration. The secondary population originates from smaller z -values. The particles have
 406 completed a full gyration from the upstream to the observation point and pass through
 407 the upstream region close to the nucleus. Probes 2-5 (panel b) contain most of the the
 408 back-traced particles of the main population. The shape of the distribution is similar to
 409 that of the main population at P3 (Figure 4). The upstream VDF of the secondary pop-
 410 ulation is mostly captured by probe 6, but parts of the distribution are seen in probes
 411 5 and 7.

412 Sampling location P5, upstream of the proton density enhancement structure, is
 413 shown in Figure 6. The main population appears only deflected, while the secondary pop-
 414 ulation shows significant gyration. Contrary to the previous two figures, the secondary
 415 population originates from larger z -values compared to the main population. Probe 3
 416 shows a broad distribution of observed velocities, which is probably due to a mixture of
 417 both populations. The major axis of the elongated distributions in probes 4-7 are not
 418 vertical but are rotated by about 20° .

419 Figure 7 shows the back-tracing results of the alpha particles at A2 (the alpha par-
 420 ticle density enhancement region). The overall structure is comparable to the protons
 421 at P5 and P6 (Figure 6). The two different populations separate by their upstream ori-

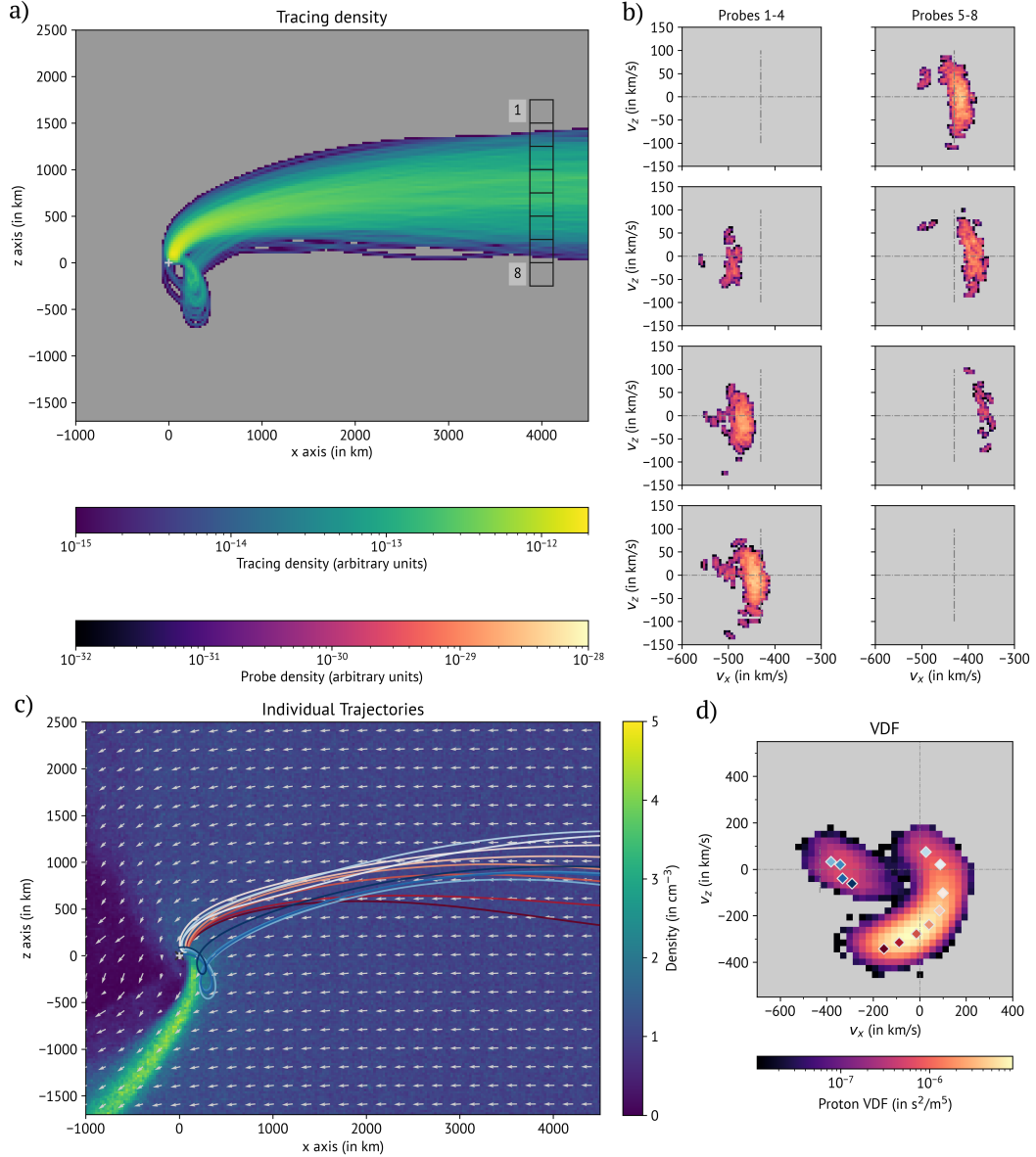


Figure 4. Particle tracing results of box P3 (protons), initial Amitis time step: 300k. Panel a: Density map of all initial particles in the x – z plane, integrated over the entire y -axis. The boxes around $x = 4000$ km mark probe locations for the back tracing VDFs (see panel b). The probes are labelled by descending z -coordinate, with probe 1 at the top. Panel b: VDFs of the back-traced particles for different probe locations (see panel a). Only the particles that pass through P3 are included; the complete VDF at this point is Maxwellian. The dash-dotted lines indicate the mean upstream SW velocity. Panel c: Background: proton density and mean velocity. Overlay: individual trajectories of selected particles. The corresponding initial velocity for each particle is shown in panel d (indicated by marker/line colours).

422 gin. The secondary population originates from larger z in the $+E$ hemisphere. The upstream
 423 VDFs of the main population (Panel b, probes 4-8) are rotated about 50° from
 424 the vertical axis, which is even more than the protons at P5. Apart from the rotation

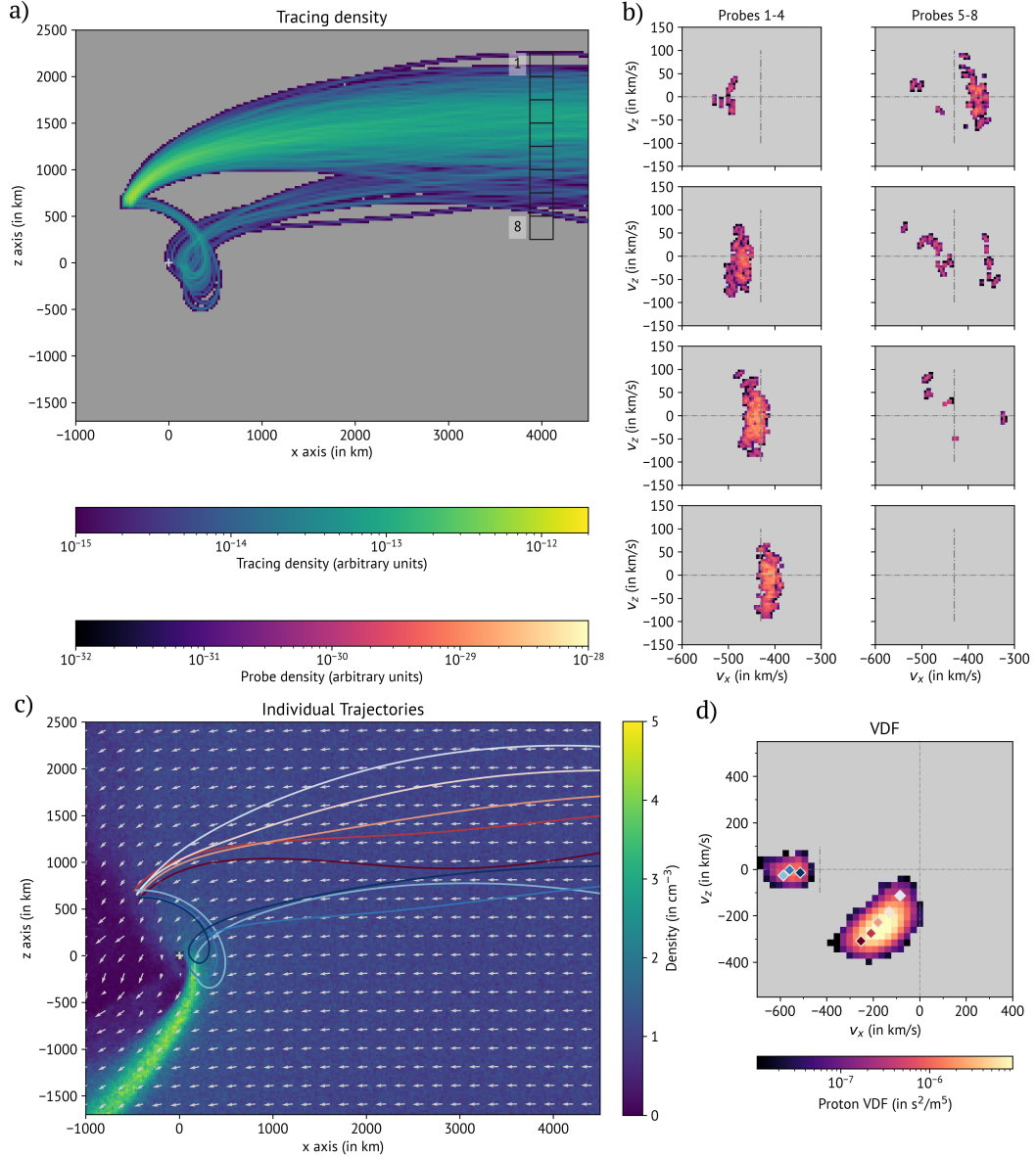


Figure 5. Particle tracing results of P1 (protons). For panel description see Figure 4.

425 the alpha VDFs are similar to the SW protons. The individual probe VDFs appear shifted
 426 perpendicular to their major axis towards $+v_x/+v_z$ for decreasing z .

427 3.3.2 Cometary Ions

428 For the cometary ions we compiled all three sampling locations (C1 - C3) into one
 429 figure (see Figure 8). The top row shows the back-tracing trajectories, and the bottom
 430 row shows the corresponding initial velocities for the illustrated trajectories. The columns
 431 show C1 (left), C2 (middle), and C3 (right), respectively. The electric field in the back-
 432 ground of the top panels is the initial electric field that is used for the particle tracing;
 433 it does not include the resistive term ($\eta\mathbf{J}$) from the hybrid model. The termination point
 434 of the particle trajectories is the location where the particle had its lowest energy dur-
 435 ing back-tracing. This should roughly correspond to the location where they are born.

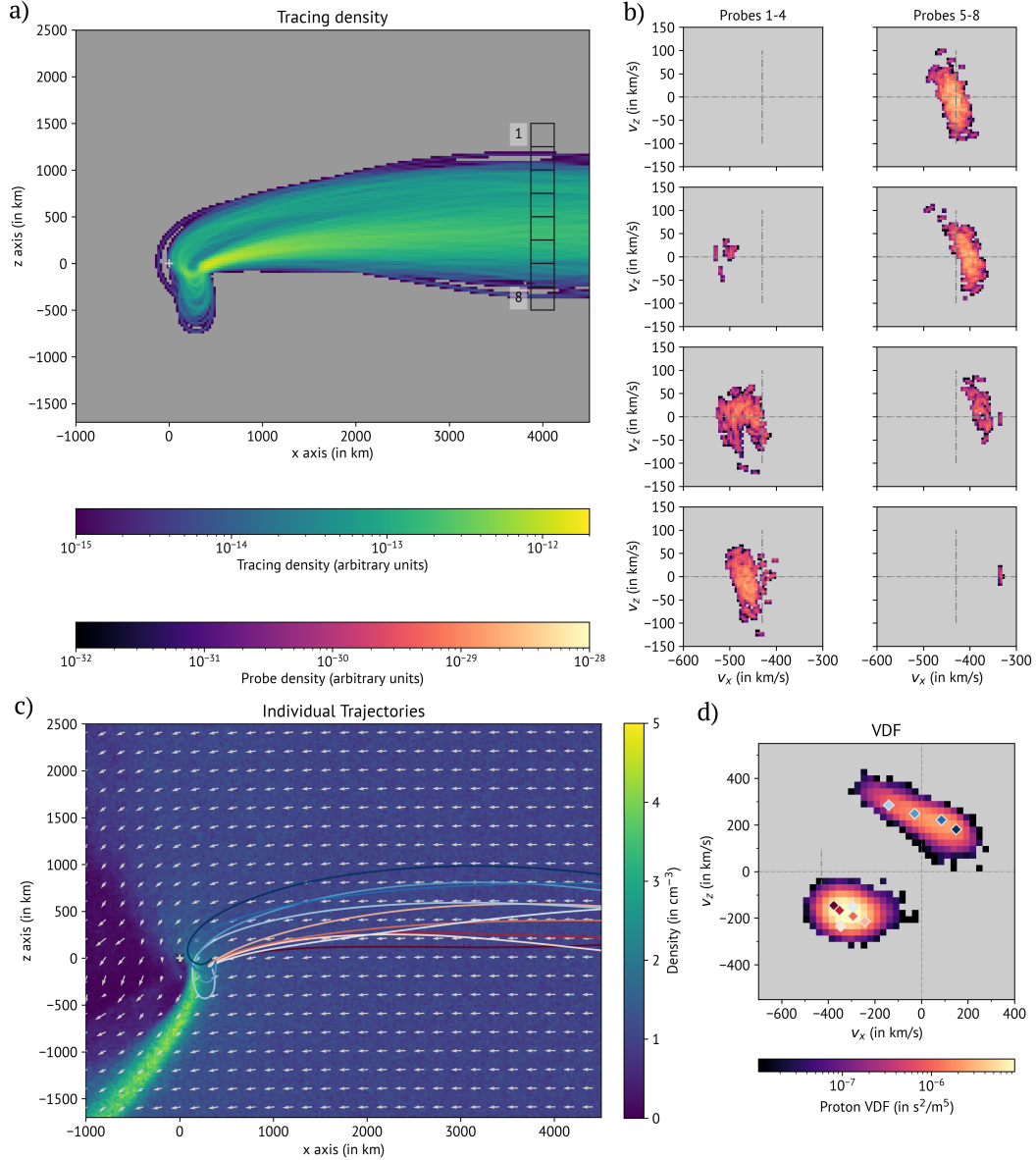


Figure 6. Particle tracing results of P5 (protons). For panel description see Figure 4.

436 We note that the cometary ions born outside the y_0 plane are in general deflected to-
 437 wards y_0 , which is opposite to the flow of solar wind particles. The back-tracing is done
 438 using time-variable fields. This means that the electric field affecting the newborn par-
 439 ticles may be different to what is shown in Figure 8.

440 At sampling point C1 (left column) particles with speeds up to 120 km/s are pre-
 441 dominantly driven by the structure of the electric field. The two different branches visible
 442 in the VDF relate two slightly different groups of trajectories. Above 120 km/s the
 443 gyration pattern of the ions becomes more important (see light blue trajectory). At C2
 444 (middle column) the trajectories can be split up in three different groups. Ions up to 70 km/s
 445 originate from the region with low electric field strength downstream of the nucleus. Par-
 446 ticles with velocities above 100 km/s originate in the undisturbed solar wind and show
 447 the typical pickup-ion distribution. They are further accelerated by the electric field en-

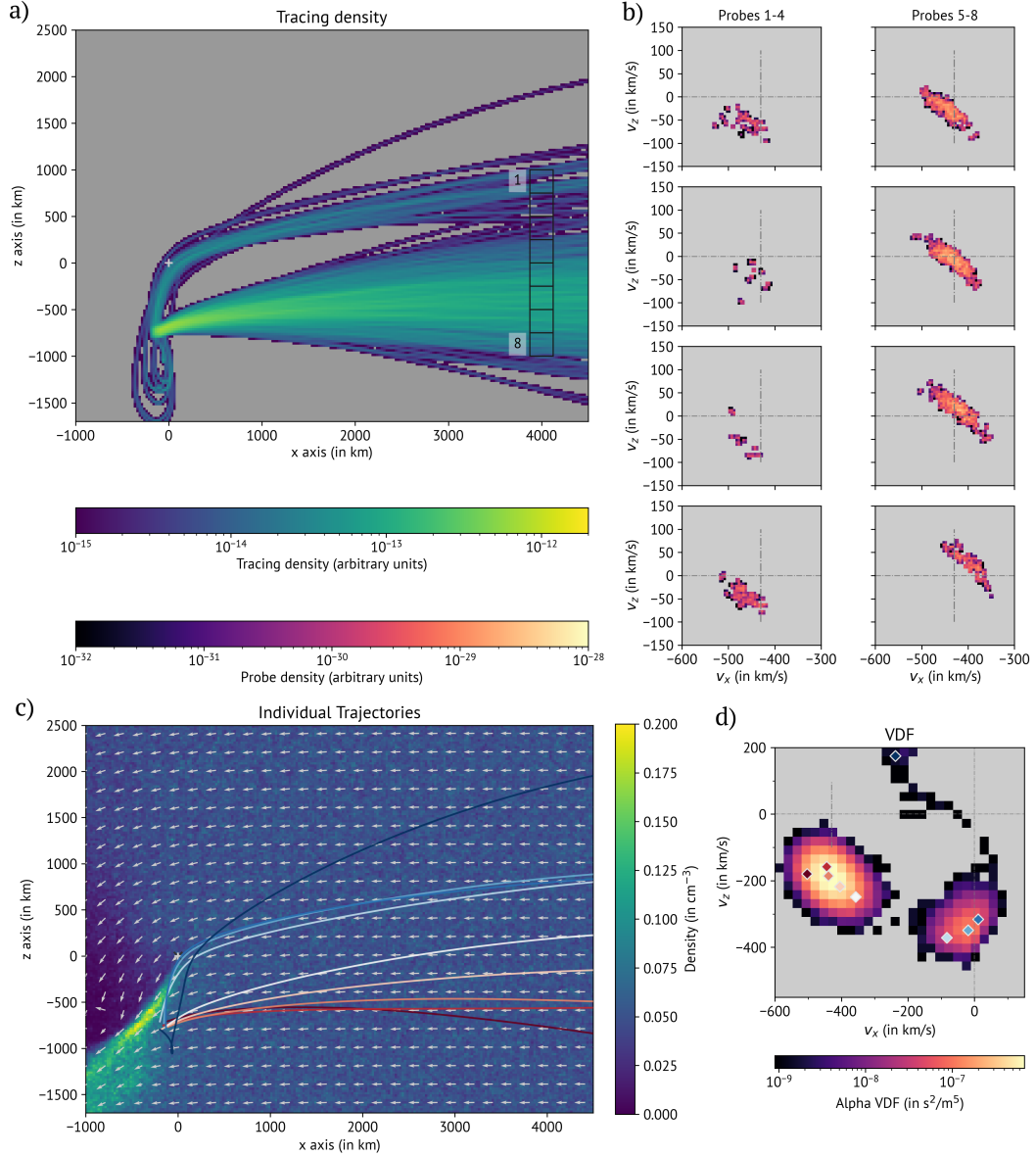


Figure 7. Particle tracing results of A2 (alpha particles). For panel description see Figure 4. Panel c, background: alpha particle density and mean velocity.

448 enhancement region they pass through. In the velocity range between 70 km/s and 100 km/s
 449 the ions originate from upstream the nucleus but do not directly pass through the elec-
 450 tric field enhancement region. The back-traced trajectories from C3 (right column) show
 451 two distinct groups of trajectories for the two distinct populations in the VDF. Ions with
 452 initial velocities $v_z > 0$ all come from the $-z$ direction. The transition between the two
 453 different circular arcs of the VDF seems to coincide with the ions originating from the
 454 undisturbed SW (higher velocities) or the electric field enhancement region (lower vel-
 455 ocities). The arc below $v_z \approx 100$ km/s appears to result from the electric field in the
 456 enhancement region, not from a partially developed gyration of the particles. The sec-
 457 ond population ($v_z < 0$) originates from a completely different region, close to the nu-
 458 cleus.

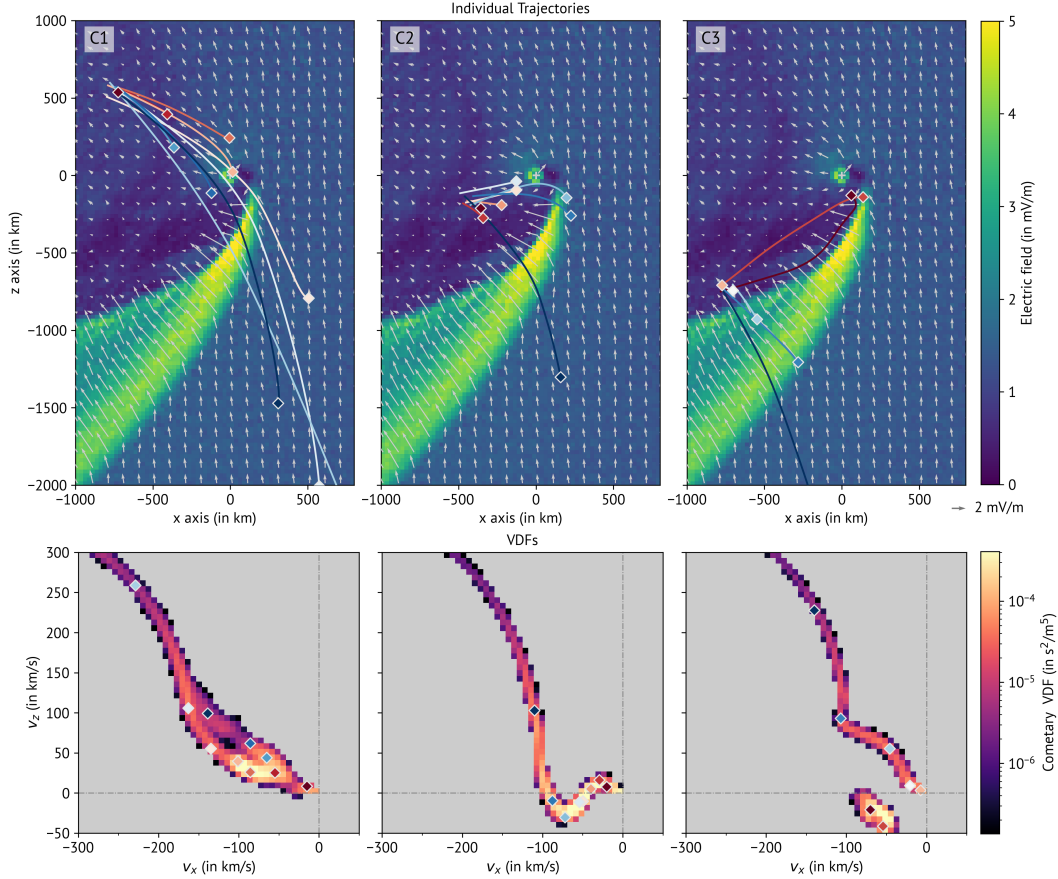


Figure 8. Particle tracing results of cometary ions (C1 - C3), projected onto the $x - z$ plane. Upper row: Background: electric field strength and direction ($E_x - E_z$ only) at $y = 0$ used for the particle tracing. Overlaid: individual particle trajectories from the three box origins C1-C3 (from left to right). The trajectories are terminated at the lowest velocity point ($v \approx 0$). Lower row: VDFs and corresponding initial particle velocities for the three box locations C1-C3.

459

4 Discussion

460

461

462

463

464

465

466

For the discussion we will retain the distinction between the $+E$ (for $z > 0$) and the $-E$ (for $z < 0$) hemispheres, but since this definition is based on the upstream parameters of the plasma, it is not sufficient to cover all observed features. We therefore introduce a third region, the “central tail”, which is the region where the cometary plasma dominates. This roughly spans the area from the nucleus towards $-x$ within a 35° cone. The solar wind ions in this region have retained none of their upstream parameters and the density is heavily depleted.

467

468

469

470

471

472

473

474

475

The plasma in the y_0 plane forms an asymmetric, half-open induced magnetosphere. In the $-E$ hemisphere an obstacle similar to a planetary bow shock is formed: a steep increase in the magnetic field strength and an enhancement of the SW density along with its deflection around the obstacle. Upstream of the boundary we observe protons that have been reflected from the boundary. Similar reflected SW ions have been reported at Mars’ bow shock (Madanian et al., 2020) as well as Earth’s bow shock at low mach numbers (Graham et al., 2024). The electric field in the proton reference frame is directed outwards, away from the obstacle towards $+x/-z$. The $+E$ hemisphere provides one of the two main escape paths for cometary ions. SW protons may enter the central tail

476 region via this path. The second escape path for cometary ions is via the central tail.
 477 The $+E$ hemisphere is more susceptible to wave generation compared to the $-E$ hemi-
 478 sphere.

479 4.1 Spatial Structure

480 The asymmetry between the $+E$ and the $-E$ hemispheres is seen both in parti-
 481 cle and in field data. In the $-E$ hemisphere the proton and alpha particle densities form
 482 a clear plasma boundary. The proton and alpha density enhancements are created by
 483 the deflection of particles towards $-z$ in order to conserve momentum due to the towards
 484 $+z$ accelerating cometary ions. The focusing of the flow lines is the primary cause for
 485 the sudden increase of the solar wind densities, since there is no significant deceleration
 486 of the flow as it approaches the boundary.

487 We can compare the relative enhancement of the proton density (≈ 4 times) and
 488 the magnetic field strength ($\approx 4-5$ times) with respect to the upstream plasma. The
 489 similar values indicate that the flow line compression and corresponding increase in den-
 490 sity is the main driving factor behind the magnetic field pile-up in this region. The elec-
 491 tric field structure in this region is still dominated by the convective electric field of the
 492 SW protons. Its increase in strength is due to the increased magnetic field strength, while
 493 the change in direction results from the deflection of the SW protons. The width of the
 494 proton density enhancement region (about 200 km across the boundary where the rela-
 495 tive density increase is at least a factor of 3.5) is the result of the deflection geometry
 496 and the local velocity distribution. The deflection is spread out over a large spatial scale
 497 due to the finite gyroradius of the ions, which puts a lower limit on the width of this bound-
 498 ary. Additionally, the protons have a significant spread in velocity (see e.g. Figure 3;
 499 Panel P6). A perpendicular speed of just 50 km/s relative to the bulk flow in the bound-
 500 ary corresponds to a gyroradius of 35 km perpendicular to the boundary. Towards $-x$
 501 downstream of the peak proton density the protons do not disappear completely, despite
 502 their mean velocities being directed parallel to the boundary. Those protons may be of
 503 different origins:

- 504 1. Protons that diffuse through the boundary. These may either be protons with higher
 505 velocities than the bulk SW proton flow, or those that have previously been re-
 506 flected at the boundary and have now gained sufficient energy to pass through.
- 507 2. Protons entering through the $+E$ hemisphere. The majority of this flow is deflected
 508 out of the y_0 plane, so what remains are tails of the bulk population.

509 A more in-depth discussion of this can be found in Sections 4.2 and 4.3 which discuss
 510 the details of the VDFs and the particle tracing.

511 The shift of the location of the alpha density enhancement towards $-x$ (and to a
 512 lesser extent $-z$) can be explained by the higher inertia (higher m/q) of the alpha par-
 513 ticles. The gyroradii of the alpha particles are larger than the proton gyroradii, and there
 514 is less deflection in the flow of alpha particles. This creates a difference between the mean
 515 velocities of protons and alpha particles, and the corresponding reference frames differ.
 516 In the local reference frame of the alpha particles there is an electric field over the pro-
 517 ton density enhancement region which accelerates the alpha particles instead of decel-
 518 erating them. There is an energy transfer from the solar wind protons to the alpha par-
 519 ticles in this region, and the alpha particles create an obstacle to the protons due to their
 520 difference in gyroradius. This effect is only relevant if the spatial scales of the bound-
 521 aries are similar to the gyroradii of the solar wind species. The consequences of differ-
 522 ent alpha/proton ratios on the boundary formation in such a case are difficult to pre-
 523 dict but should be investigated further in the future.

524 No clear plasma boundaries are visible in the $+E$ hemisphere. The changes in the
 525 plasma environment are more gradual. There is no visible focussing of the SW protons
 526 or alpha particles in the y_0 plane. A stationary focussing of protons or alphas into the
 527 y_0 plane is highly unlikely since there is no force pushing the SW ions back towards y_0 .
 528 Thus, any density enhancement must be due to a local deceleration of the mean parti-
 529 cle flow, or the result of asymmetries along the y -axis.

530 Close to the nucleus at $+x/+z$ the increase in magnetic field strength is a result
 531 of the deceleration of the solar wind, and the addition of mass in form of cold, newborn
 532 cometary ions. This in turn decelerates the local electron fluid and results in the mag-
 533 netic field pile-up in this region. Further away from the nucleus in the $+E$ hemisphere
 534 the magnetic field remains enhanced because the plasma is more and more dominated
 535 by the cometary plasma. The magnetic field transitions from being frozen into the SW
 536 plasma to being frozen into the cometary plasma, and the flow of cometary ions increas-
 537 ingly shapes the structure of the magnetic and electric field.

538 In general the $+E$ hemisphere shows much more variation of the plasma structures
 539 in time and space. We interpret this as the result of wave activity. This affects the mag-
 540 netic field, the protons (especially in the density), and the cometary ions (data not shown).
 541 For the alpha particles the spatial scales in this simulation are probably too small to al-
 542 low for the development of wave activity. The shielded region directly upstream of the
 543 nucleus may be formed by a polarisation electric field that partially cancels the solar wind
 544 electric field, as proposed by Nilsson et al. (2018). By analysing the VDFs of accelerated
 545 cometary ions in this region, Moeslinger, Nilsson, et al. (2023) reported an average elec-
 546 tric field strength of 0.21 mV/m, very similar to the minimum values found in our sim-
 547 ulations.

548 4.2 VDFs

549 Comparing the VDFs of any of the three species at any location within the comet
 550 magnetosphere (Figure 3) with their mean velocity counterparts (Figure 1a-c) shows just
 551 how much information is lost when only considering the latter. We use the VDFs to study
 552 deviations from a Maxwellian in the bulk populations and identify secondary popula-
 553 tions. While the details of the particle trajectories are discussed in Section 4.3 below we
 554 emphasise that the evolution of VDFs is due to the particle trajectories. In both SW species
 555 we never see a formation of a gyrotropic plasma, even in its infancy stage. This is be-
 556 cause all structures in the magnetosphere that strongly influence the particle motion are
 557 smaller than or of the same size as the particle gyroradius. While there is gyration of
 558 each particle that has non-zero velocity in the upstream solar wind reference frame, we
 559 only consider gyration that occurs due to the interaction with the comet. In this con-
 560 text we use the word deflection to describe small angular changes ($< 90^\circ$) in velocity,
 561 while gyration refers to large angular changes in velocity and the corresponding cycloid
 562 trajectories. Angular changes are defined as the angle between the upstream SW direc-
 563 tion ($\mathbf{v} = (-430, 0, 0)$ km/s), 0 velocity (in the comet reference frame), and the observed
 564 velocity in a mathematically positive way (counter-clockwise).

565 The majority of protons in the $+E$ hemisphere are significantly decelerated, along
 566 with their deflection towards $-E$, and most of the cometary ions are accelerated along
 567 the electric field. The main source of free energy to support acceleration are the local
 568 SW protons. In theory, other regions could also provide energy to the cometary ions by
 569 wave-particle-interaction (e.g. Alfvén waves). But those mechanisms are much less ef-
 570 fective in transporting energy and are therefore not expected to significantly contribute
 571 to the energy budget. Further into the coma (towards $-x$, compare P2 to P1) the de-
 572 flection and deceleration increases as the protons are more and more influenced by the
 573 cometary ions. A minor part of the protons in the $+E$ hemisphere, seen as a secondary
 574 population, are actually accelerated. They must gain energy while passing through the

575 region with strong electric fields and gradients close to the nucleus, not following the bulk
 576 flow of protons. Once they have reached the fairly homogenous $+E$ hemisphere further
 577 downstream of the nucleus they are gyrating in the local fields. Other than their vari-
 578 ation in energy due to this gyration motion, they will only lose energy via wave-particle
 579 interaction. This is expected to only be relevant multiple full gyrations far downstream
 580 in the tail.

581 In the $-E$ hemisphere protons are not significantly decelerated, only deflected (P5
 582 and P6). They create the plasma structures in this part of the comet magnetosphere,
 583 but are not providing much energy to the cometary ions. Some of their energy, however,
 584 must go into building up the plasma structures in this region. Secondary populations
 585 are typically first seen close to the nucleus or in the $-E$ hemisphere, where they resem-
 586 ble ions reflected from a shock. They are therefore often observed as counter-streaming
 587 the main SW flow. Depending on their exact origin, they may enter the $+E$ hemisphere
 588 as their gyration progresses. Especially for these particles there is no obstacle in form
 589 of an electric field that they have to climb. Hence they retain some of the energy they
 590 gained during the gyration and are now faster than the upstream solar wind. The ions
 591 that do not enter the $+E$ hemisphere still gain enough energy to pass over the proton
 592 density enhancement.

593 The most anisotropic proton population, resembling a partial ring, is seen close to
 594 the nucleus (P3). This is the region where we have the strongest magnetic and electric
 595 fields, but also the strongest gradients in those fields. The secondary population must
 596 be generated in a similar way as in all other cases: it consists of a small portion of the
 597 upstream solar wind that has already performed a full gyration when arriving at the sam-
 598 pling location. Partial ring distributions have been observed by Rosetta in a few cases
 599 (Moeslinger, Stenberg Wieser, et al., 2023). However, the model results indicate that these
 600 partial ring-shaped proton VDFs extend at least 400 km from the nucleus in the $+E$ hemi-
 601 sphere, as well as 100 km into the $-E$ hemisphere. This is a much larger region than pre-
 602 viously thought (Moeslinger, Stenberg Wieser, et al., 2023). The VDF in the central tail
 603 (P4) does not show a clearly dominating population. The observed particles seem to be
 604 a mix of several secondary populations. We also note that of all the sampling locations
 605 shown, the central tail region shows the largest diversity and spatial change in the shape
 606 of VDFs.

607 Close to the nucleus the alpha particles did not have enough time or space to evolve
 608 into complex VDFs (A3). Due to their larger inertia the alpha particle distributions are
 609 different from the proton distributions. The small anisotropy seen is consistent with ob-
 610 servations (Moeslinger, Stenberg Wieser, et al., 2023). When the alpha particles pass the
 611 electric field enhancement caused by the protons a few hundred kilometres below the nu-
 612 cleus, their velocity has a larger anti-sunward component compared to the protons. Hence
 613 the electric field does not form a potential barrier for them. Instead it accelerates them
 614 towards $-z$. At the alpha density enhancement (A2), the main population has gained
 615 about 200 eV in energy with respect to the upstream SW plasma. This energy is indi-
 616 rectly provided by the protons via the plasma boundary. The main alpha population down-
 617 stream of the alpha density enhancement (A1) is a residual from the SW alphas enter-
 618 ing through the $+E$ hemisphere that has not yet been deflected out of the y_0 plane. The
 619 secondary population must have gone through a full gyration before the observation point.

620 The high velocity part of the cometary ion VDFs (C1 - C3) is a partial ring formed
 621 by the classical pickup process. The high speeds as well as the circular shape indicate
 622 that these ions were born far away from the observation point and have been acceler-
 623 ated in the undisturbed solar wind. Without additional electric field structures (apart
 624 from the undisturbed solar wind) the partial ring would start very close to $\mathbf{v} = (0, 0, 0)$.
 625 The offset of the ring structure is created by the inhomogeneous electric field around the
 626 nucleus. The lower velocity part of the distribution is formed by ions born closer to the

627 observation point. Interpreting their more complex shapes is only possible with the help
628 of the particle back-tracing results.

629 Anisotropic VDFs are inherently unstable. As the plasma evolves further away from
630 the comet, the observed anisotropies in the VDFs will eventually relax back to Maxwellian-
631 shaped distributions. The fully picked-up ring distributions of cometary ions will pitch-
632 angle scatter into shells, which will eventually thermalise by energy diffusion (Coates et
633 al., 1989). This process takes place over many gyrations and cannot be observed in our
634 simulations due to the spatial limits of the tail downstream. The partial-ring-shaped VDFs
635 of protons, and to a lesser extent alpha particles, can be interpreted as temperature anisotropies,
636 or nongyrotropic distributions. Temperature anisotropies can result in the generation
637 of mirror-mode waves which have been observed at comet 67P (Volwerk et al., 2016; Tello Fal-
638 lau et al., 2023) and comet 1P/Halley (Russell et al., 1987; Schmid et al., 2014). How-
639 ever, all of these observations have associated the observed mirror modes with temper-
640 ature anisotropies of cometary water group ions, not solar wind protons. Phase-space
641 diffusion of nongyrotropic ion distributions has been studied for example by Motschmann
642 et al. (1997). Typical diffusion timescales, that is, the time until the nongyrotropic VDFs
643 relax back to a Maxwellian equilibrium, are of the order of 10 gyroperiods, but some dif-
644 fusion should already be visible after only one gyration. This may be one reason why
645 the partial ring distributions are most pronounced close to the nucleus.

646 4.3 Particle Tracing

647 Particle tracing of the solar wind ions confirms that the observed particles close
648 to the nucleus are on their first gyration from the upstream origin where they are ini-
649 tialised as isotropic solar wind in the simulation. The width (extent in the z direction)
650 of the upstream origin area of SW protons is larger for P3 (close to the nucleus) than
651 for the sampling locations P1 and P6. This is consistent with the wider spread in phase
652 space of the main population at point P3. The energy of the particles at the observa-
653 tion point depends on their energy upstream, which is limited by the upstream veloc-
654 ity and temperatures, and how much they have moved with or against the electric field.
655 The displacement in the electric field depends on the path of the individual particles and
656 varies for particles of the main population for different observed velocities due to their
657 different upstream origin. Ions from higher up along the z -axis have lost more energy
658 if the overall deflection is towards $-z$. Since particles from the secondary populations
659 have passed through the highly inhomogeneous E -field region close to the nucleus their
660 energies can change drastically compared to the main population. The origin of the main
661 populations vary quite a lot between different sampling locations. Sampling locations
662 at a higher z position also tend to have upstream origins from higher z . The upstream
663 origin of the secondary location on the other hand seems to be within $0 < z < 500$ km
664 for all particle trajectories analysed. Therefore, the secondary populations observed in
665 all the proton VDFs are created in a similar manner but then evolve into different re-
666 gions. We note that at more negative z values than analysed here secondary populations
667 may still be created at the plasma boundary although the reflection geometry may be
668 different.

669 The correlation between the level of deflection or gyration of the protons seen in
670 the VDFs and the actual spatial gyration pattern is quite clear. It is possible to get a
671 good approximation of the particle paths by taking the respective VDF and comparing
672 it with the tracing patterns. Details are difficult to predict and still require the parti-
673 cle tracing for interpretation. The back-tracing also reveals the effects of the higher in-
674 ertia of the alpha particles (Figure 7). The secondary population has been significantly
675 deflected close to the nucleus where the fields are the strongest, but otherwise the de-
676 flection is more gradual. This was consistently observed in the back-tracing of several
677 alpha particle VDFs, including the one shown here. From the upstream VDF probes (Fig-

ures 4 - 6, Panel b) we can see that the v_x component is much more important than the v_z component when it comes to correlating upstream location and upstream VDF shape.

For the cometary ions, particle gyration only seems to become relevant for ions with observed velocities above ≈ 150 km/s. The backtracing of these higher velocity ions shows that they are indeed born in the undisturbed solar wind at various distances from the observation location, with higher energetic particles originating further away from the observation point. For ions with velocities below 100 – 150 km/s the structure of the electric field is much more important for the resulting VDFs than any gyration motion. Any curvature in the low-velocity part of the VDFs (especially C3 in the $-v_x/+v_z$ quadrant) is not due to a gyration in the magnetic field but purely due to a structure in the electric field. The trajectories of these particles appear fairly straight and change in upstream origin location. If they were indeed due to a gyration in the magnetic field the curvature of the trajectories should be more pronounced. Steep gradients in the electric field result in sudden changes in the shape of the VDF. They do, however, not necessarily result in isolated populations. If such an isolated population is seen in the VDF it is a strong indicator that there are two unrelated paths from two separate regions in the cometosphere available for the cometary ions to take to the observation point.

5 Conclusions

In our simulations the plasma environment around a comet akin to comet 67P at larger heliocentric distances takes the shape of a half-open induced magnetosphere. Apart from the asymmetries in the $+E$ and $-E$ hemispheres often associated with such low-outgassing scenarios, we find that there is a formation of plasma boundaries in the $-E$ hemisphere. The $+E$ hemisphere lacks such clear boundaries, but provides an escape path for the cometary ions and is more susceptible to wave activity. Close to the nucleus strong electric and magnetic fields lead to highly anisotropic velocity distribution functions in the solar wind proton data, which resemble partial rings. Some protons of this anisotropic VDF split away from the bulk flow and are observed as secondary populations in both hemispheres. Similar distributions (partial rings with a secondary population) have previously been identified in Rosetta measurements of solar wind protons (Moeslinger, Stenberg Wieser, et al., 2023). Solar wind alpha particles form VDFs with two populations further downstream, but they require a larger interaction region due to their higher inertia. Dynamic particle back-tracing aids in understanding the VDFs of all species, but is especially important for understanding the origin of cometary ions at a given location. The VDFs of cometary ions are mainly driven by electric field structures for velocities up to 100 – 150 km/s.

Appendix A Data Availability Statement

Additional simulation results are included in the Supporting Information of this paper. The code used for particle tracing has been made publicly available (see Moeslinger & Gunell, 2024). Data analysis was done using NumPy version 1.20.2 (Harris et al., 2020). Figures were made using Matplotlib (Caswell et al., 2021; Hunter, 2007).

Acknowledgments

The simulations were enabled by resources provided by the National Academic Infrastructure for Supercomputing in Sweden (NAISS) at High Performance Computing Center North (HPC2N) partially funded by the Swedish Research Council through grant agreement no. 2022-06725. Work at the Swedish Institute of Space Physics in Kiruna (IRF) was funded by the Swedish National Space Agency (SNSA) grant 132/19. Work at Umeå university was supported by SNSA grant 2023-00208 (HG) and SNSA grant 2022-00183 (SF).

References

- 726
- 727 Aizawa, S., Griton, L., Fatemi, S., Exner, W., Deca, J., Pantellini, F., . . . Usui,
728 H. (2021, April). Cross-comparison of global simulation models applied to
729 Mercurys dayside magnetosphere. *Planetary and Space Science*, *198*, 105176.
730 Retrieved 2024-04-04, from [https://linkinghub.elsevier.com/retrieve/
731 pii/S0032063321000155](https://linkinghub.elsevier.com/retrieve/pii/S0032063321000155) doi: 10.1016/j.pss.2021.105176
- 732 André, M., & Yau, A. W. (1997). Theories and observations of ion energization and
733 outflow in the high latitude magnetosphere. *Space Sci. Rev.*, *80*, 27–48.
- 734 Behar, E., Nilsson, H., Alho, M., Goetz, C., & Tsurutani, B. (2017). The birth
735 and growth of a solar wind cavity around a comet - rosetta observations.
736 *Monthly Notices of the Royal Astronomical Society*, *469*, S396-S403. doi:
737 10.1093/mnras/stx1871
- 738 Behar, E., Nilsson, H., Wieser, G. S., Nemeth, Z., Broiles, T. W., & Richter, I.
739 (2016, February). Mass loading at 67P/Churyumov-Gerasimenko: A case
740 study. *Geophys. Res. Lett.*, *43*, 1411-1418. doi: 10.1002/2015GL067436
- 741 Biermann, L., Brosowski, B., & Schmidt, H. U. (1967). The interaction of the solar
742 wind with a comet. *Solar Physics*, *1*(2), 254-284. doi: 10.1007/BF00150860
- 743 Boris, J. P. (1970, 11). Relativistic plasma simulation-optimization of a hybrid
744 code. In *Proceedings: Fourth conference on numerical simulation of plasmas*
745 (p. 3-67). Naval Research Laboratory.
- 746 Broiles, T. W., Burch, J. L., Clark, G., Goeters, C., Behar, E., Goldstein, R., . . .
747 Samara, M. (2015, November). Rosetta observations of solar wind interaction
748 with the comet 67P/Churyumov-Gerasimenko. *Astronomy and Astrophysics*,
749 *583*, A21. doi: 10.1051/0004-6361/201526046
- 750 Caswell, T. A., Lee, M. D. A., de Andrade, E. S., Hunter, J., Hoffmann, T., Firing,
751 E., . . . Ivanov, P. (2021). *matplotlib/matplotlib: REL: v3.4.1* [software]. Re-
752 trieved from <https://github.com/matplotlib/matplotlib/tree/v3.4.1>
753 doi: 10.5281/zenodo.4649959
- 754 Coates, A. J., Johnstone, A. D., Wilken, B., Jockers, K., & Glassmeier, K.-H. (1989,
755 8). Velocity space diffusion of pickup ions from the water group at comet Hal-
756 ley. *Journal of Geophysical Research: Space Physics*, *94*, 9983-9993. doi: 10
757 .1029/ja094ia08p09983
- 758 Edberg, N., Eriksson, A. I., Vigren, E., Nilsson, H., Gunell, H., Götz, C., . . .
759 De Keyser, J. (2024). Scale size of cometary bow shocks. *Astronomy and*
760 *Astrophysics, Proposed for acceptance October 2023*.
- 761 Fatemi, S., Poppe, A. R., Delory, G. T., & Farrell, W. M. (2017, May). AMITIS: A
762 3D GPU-Based Hybrid-PIC Model for Space and Plasma Physics. In *Journal*
763 *of Physics: Conference Series* (Vol. 837). Institute of Physics Publishing. (Is-
764 sue: 1 ISSN: 17426596) doi: 10.1088/1742-6596/837/1/012017
- 765 Fatemi, S., Poppe, A. R., Vorburger, A., Lindkvist, J., & Hamrin, M. (2022, Jan-
766 uary). Ion Dynamics at the Magnetopause of Ganymede. *Journal of Geo-*
767 *physical Research: Space Physics*, *127*(1), e2021JA029863. Retrieved 2024-
768 04-03, from [https://agupubs.onlinelibrary.wiley.com/doi/10.1029/
769 2021JA029863](https://agupubs.onlinelibrary.wiley.com/doi/10.1029/2021JA029863) doi: 10.1029/2021JA029863
- 770 Galand, M., Héritier, K. L., Odelstad, E., Henri, P., Broiles, T. W., Allen, A. J., . . .
771 Wurz, P. (2016). Ionospheric plasma of comet 67P probed by Rosetta at 3
772 au from the Sun. *Monthly Notices of the Royal Astronomical Society*, *462*,
773 S331-S351. doi: 10.1093/mnras/stw2891
- 774 Glassmeier, K.-H., Boehnhardt, H., Koschny, D., Kührt, E., & Richter, I. (2007).
775 The Rosetta Mission: Flying Towards the Origin of the Solar System. *Space*
776 *Science Reviews*, *128*(1-4), 1-21. Retrieved from [http://dx.doi.org/
777 10.1007/s11214-006-9140-8](http://dx.doi.org/10.1007/s11214-006-9140-8) doi: 10.1007/s11214-006-9140-8
- 778 Goetz, C., Behar, E., Beth, A., Bodewits, D., Bromley, S., Burch, J., . . . Volw-
779 erk, M. (2022, 12). The Plasma Environment of Comet 67P/Churyumov-
780 Gerasimenko. *Space Science Reviews*, *218*. doi: 10.1007/s11214-022-00931-1

- 781 Goetz, C., Gunell, H., Johansson, F., Llera, K., Nilsson, H., Glassmeier, K. H., &
782 Taylor, M. G. (2021, 5). Warm protons at comet 67p/churyumov-gerasimenko-
783 implications for the infant bow shock. *Annales Geophysicae*, *39*, 379-396. doi:
784 10.5194/angeo-39-379-2021
- 785 Graham, D. B., Khotyaintsev, Y. V., Dimmock, A. P., Lalti, A., Bold, J. J., Tigik,
786 S. F., & Fuselier, S. A. (2024, April). Ion Dynamics Across a Low Mach
787 Number Bow Shock. *Journal of Geophysical Research: Space Physics*,
788 *129*(4), e2023JA032296. Retrieved 2024-04-16, from [https://doi.org/](https://doi.org/10.1029/2023JA032296)
789 10.1029/2023JA032296 (Publisher: John Wiley & Sons, Ltd) doi:
790 10.1029/2023JA032296
- 791 Gunell, H., Goetz, C., & Fatemi, S. (2024). Impact of radial interplanetary mag-
792 netic fields on the inner coma of comet 67p/churyumov-gerasimenko - hybrid
793 simulations of the plasma environment. *Astronomy and Astrophysics*, *682*,
794 A62. Retrieved from <https://doi.org/10.1051/0004-6361/202348186> doi:
795 10.1051/0004-6361/202348186
- 796 Gunell, H., Goetz, C., Simon Wedlund, C., Lindkvist, J., Hamrin, M., Nilsson, H.,
797 ... Holmström, M. (2018). The infant bow shock: a new frontier at a weak
798 activity comet. *A&A*, *619*, L2. Retrieved from [https://doi.org/10.1051/](https://doi.org/10.1051/0004-6361/201834225)
799 0004-6361/201834225 doi: 10.1051/0004-6361/201834225
- 800 Gunell, H., Mann, I., Wedlund, C. S., Kallio, E., Alho, M., Nilsson, H., ... Mag-
801 giolo, R. (2015, 12). Acceleration of ions and nano dust at a comet in
802 the solar wind. *Planetary and Space Science*, *119*, 13-23. doi: 10.1016/
803 j.pss.2015.08.019
- 804 Harris, C. R., Millman, K. J., van der Walt, S. J., Gommers, R., Virtanen, P., Cour-
805 napeau, D., ... Oliphant, T. E. (2020, September). Array programming with
806 NumPy. *Nature*, *585*(7825), 357-362. Retrieved from [https://doi.org/](https://doi.org/10.1038/s41586-020-2649-2)
807 10.1038/s41586-020-2649-2 doi: 10.1038/s41586-020-2649-2
- 808 Haser, L. (1957, January). Distribution d'intensité dans la tête d'une comète. *Bul-*
809 *letin de la Societe Royale des Sciences de Liege*, *43*, 740-750.
- 810 Holmström, M., Fatemi, S., Futaana, Y., & Nilsson, H. (2012). The interaction be-
811 tween the moon and the solar wind. *Earth, Planets, Space*, *64*, 237-245. doi:
812 <https://doi.org/10.5047/eps.2011.06.040>
- 813 Hunter, J. D. (2007). Matplotlib: A 2d graphics environment. *Computing in Science*
814 *& Engineering*, *9*(3), 90-95. doi: 10.1109/MCSE.2007.55
- 815 Jones, G. H., Snodgrass, C., Tubiana, C., Kppers, M., Kawakita, H., Lara, L. M.,
816 ... Ji, H. (2024, February). The Comet Interceptor Mission. *Space Science*
817 *Reviews*, *220*(1), 9. Retrieved 2024-04-08, from [https://link.springer.com/](https://link.springer.com/10.1007/s11214-023-01035-0)
818 10.1007/s11214-023-01035-0 doi: 10.1007/s11214-023-01035-0
- 819 Koenders, C., Perschke, C., Goetz, C., Richter, I., Motschmann, U., & Glassmeier,
820 K. H. (2016, 10). Low-frequency waves at comet 67p/churyumov-gerasimenko:
821 Observations compared to numerical simulations. *Astronomy and Astrophysics*,
822 *594*. doi: 10.1051/0004-6361/201628803
- 823 Ledvina, S. A., Ma, Y.-J., & Kallio, E. (2008, August). Modeling and Simulating
824 Flowing Plasmas and Related Phenomena. *Space Science Reviews*, *139*(1-4),
825 143-189. Retrieved 2024-03-05, from [http://link.springer.com/10.1007/](http://link.springer.com/10.1007/s11214-008-9384-6)
826 s11214-008-9384-6 doi: 10.1007/s11214-008-9384-6
- 827 Madanian, H., Schwartz, S. J., Halekas, J. S., & Wilson, L. B. (2020, June). Non-
828 stationary Quasiperpendicular Shock and Ion Reflection at Mars. *Geophysical*
829 *Research Letters*, *47*(11). (Publisher: Blackwell Publishing Ltd) doi: 10.1029/
830 2020GL088309
- 831 Mandt, K. E., Eriksson, A., Edberg, N. J. T., Koenders, C., Broiles, T., Fuselier,
832 S. A., ... Stenberg Wieser, G. (2016). Rpc observation of the develop-
833 ment and evolution of plasma interaction boundaries at 67p/churyumov-
834 gerasimenko. *Monthly Notices of the Royal Astronomical Society*, *462*, S9-S22.
835 doi: 10.1093/mnras/stw1736

- 836 Moeslinger, A., & Gunell, H. (2024). *Particle Tracing Code* [software]. Zenodo.
 837 Retrieved from <https://doi.org/10.5281/zenodo.10973547> doi: 10.5281/
 838 zenodo.10973547
- 839 Moeslinger, A., Nilsson, H., Stenberg Wieser, G., Gunell, H., & Goetz, C. (2023,
 840 September). Indirect Observations of Electric Fields at Comet 67P. *Journal of*
 841 *Geophysical Research: Space Physics*, *128*(9), e2023JA031746. Retrieved 2024-
 842 04-05, from [https://agupubs.onlinelibrary.wiley.com/doi/10.1029/](https://agupubs.onlinelibrary.wiley.com/doi/10.1029/2023JA031746)
 843 [2023JA031746](https://agupubs.onlinelibrary.wiley.com/doi/10.1029/2023JA031746) doi: 10.1029/2023JA031746
- 844 Moeslinger, A., Stenberg Wieser, G., Nilsson, H., Gunell, H., Williamson, H. N.,
 845 Llera, K., ... Richter, I. (2023, 2). Solar Wind Protons Forming Partial Ring
 846 Distributions at Comet 67P. *Journal of Geophysical Research: Space Physics*,
 847 *128*. doi: 10.1029/2022JA031082
- 848 Motschmann, U., Kafemann, H., & Scholer, M. (1997, June). Nongyrotropy in mag-
 849 netoplasmas: simulation of wave excitation and phase-space diffusion. *Annales*
 850 *Geophysicae*, *15*(6), 603–613. Retrieved from [https://doi.org/10.1007/](https://doi.org/10.1007/s00585-997-0603-3)
 851 [s00585-997-0603-3](https://doi.org/10.1007/s00585-997-0603-3) doi: 10.1007/s00585-997-0603-3
- 852 Neubauer, F. M., Glassmeier, K. H., Pohl, M., Raeder, J., Acuna, M. H., Burlaga,
 853 L. F., ... Schmidt, H. U. (1986, 05 15). First results from the giotto magne-
 854 tometer experiment at comet halley. *Nature*, *321*(6067s), 352–355. Retrieved
 855 from <http://dx.doi.org/10.1038/321352a0>
- 856 Nilsson, H., Gunell, H., Karlsson, T., Brenning, N., Henri, P., Goetz, C., ...
 857 Vallières, X. (2018, 8). Size of a plasma cloud matters: The polarisation
 858 electric field of a small-scale comet ionosphere. *Astronomy and Astrophysics*,
 859 *616*. doi: 10.1051/0004-6361/201833199
- 860 Nilsson, H., Wieser, G. S., Behar, E., Gunell, H., Wieser, M., Galand, M., ... Vi-
 861 gren, E. (2017, 7). Evolution of the ion environment of comet 67p during the
 862 rosetta mission as seen by rpc-ica. *Monthly Notices of the Royal Astronomical*
 863 *Society*, *469*, S252-S261. doi: 10.1093/mnras/stx1491
- 864 Russell, C. T., Riedler, W., Schwingenschuh, K., & Yeroshenko, Y. (1987,
 865 June). Mirror instability in the magnetosphere of comet Halley. *Geo-*
 866 *physical Research Letters*, *14*(6), 644–647. Retrieved 2024-04-05, from
 867 <https://doi.org/10.1029/GL014i006p00644> (Publisher: John Wiley &
 868 Sons, Ltd) doi: 10.1029/GL014i006p00644
- 869 Schmid, D., Volwerk, M., Plaschke, F., Vrs, Z., Zhang, T. L., Baumjohann, W.,
 870 & Narita, Y. (2014, June). Mirror mode structures near Venus and Comet
 871 P/Halley. *Annales Geophysicae*, *32*(6), 651–657. Retrieved 2024-04-05,
 872 from <https://angeo.copernicus.org/articles/32/651/2014/> doi:
 873 10.5194/angeo-32-651-2014
- 874 Taylor, M. G. G. T., Altobelli, N., Buratti, B. J., & Choukroun, M. (2017).
 875 The rosetta mission orbiter science overview: the comet phase. *Philo-*
 876 *sophical Transactions of the Royal Society of London A: Mathematical,*
 877 *Physical and Engineering Sciences*, *375*(2097). Retrieved from [http://](http://rsta.royalsocietypublishing.org/content/375/2097/20160262)
 878 rsta.royalsocietypublishing.org/content/375/2097/20160262 doi:
 879 10.1098/rsta.2016.0262
- 880 Tello Fallau, A., Goetz, C., Simon Wedlund, C., Volwerk, M., & Moeslinger, A.
 881 (2023, December). Revisiting mirror modes in the plasma environment of
 882 comet 67P/ChuryumovGerasimenko. *Annales Geophysicae*, *41*(2), 569–587.
 883 Retrieved 2024-04-05, from [https://angeo.copernicus.org/articles/41/](https://angeo.copernicus.org/articles/41/569/2023/)
 884 [569/2023/](https://angeo.copernicus.org/articles/41/569/2023/) doi: 10.5194/angeo-41-569-2023
- 885 Volwerk, M., Richter, I., Tsurutani, B., Gtz, C., Altwegg, K., Broiles, T., ... Glass-
 886 meier, K.-H. (2016, January). Mass-loading, pile-up, and mirror-mode waves
 887 at comet 67P/Churyumov-Gerasimenko. *Annales Geophysicae*, *34*(1), 1–15.
 888 Retrieved 2024-04-05, from [https://angeo.copernicus.org/articles/34/1/](https://angeo.copernicus.org/articles/34/1/2016/)
 889 [2016/](https://angeo.copernicus.org/articles/34/1/2016/) doi: 10.5194/angeo-34-1-2016
- 890 Wang, X.-D., Fatemi, S., Holmstrm, M., Nilsson, H., Futaana, Y., & Barabash,

891 S. (2023, 11). Martian global current systems and related solar wind en-
892 ergy transfer: hybrid simulation under nominal conditions. *Monthly Notices*
893 *of the Royal Astronomical Society*, 527(4), 12232-12242. Retrieved from
894 <https://doi.org/10.1093/mnras/stad3486> doi: 10.1093/mnras/stad3486
895 Williamson, H. N., Nilsson, H., Stenberg Wieser, G., A. Moeslinger, A., & Goetz,
896 C. (2022, 4). Development of a cometosheath at comet 67P/Churyumov-
897 Gerasimenko - A case study comparison of Rosetta observations. *A&A*, 660.
898 Retrieved from <https://doi.org/10.1051/0004-6361/202142461> doi:
899 10.1051/0004-6361/202142461